Nuclear Science and Techniques (2025) 36:1
https://doi.org/10.1007/s41365-024-01529-8

CMOS direct conversion X-ray detector coupled with fluorinated liquid

Shi-Hua Liu[1,2] · Chao-Song Gao[1] · Xin Zhang[3] · Xiang-Ming Sun[1] · Meng Wu[1] · Zhi-Hui Han[1] · Tong Wan[1] · Yong-Shuai Ge[3]

Received: 14 September 2023 / Revised: 3 February 2024 / Accepted: 28 February 2024 / Published online: 16 December 2024

Abstract

X-ray detectors show potential applications in medical imaging, materials science, and nuclear energy. To achieve high detection efficiency and spatial resolution, many conventional semiconductor materials, such as amorphous selenium, cadmium telluride zinc, and perovskites, have been utilized in direct conversion X-ray detectors. However, these semiconductor materials are susceptible to temperature-induced performance degradation, crystallization, delamination, uneven lattice growth, radiation damage, and high dark current. This study explores a new approach by coupling an FC40 electronic fluorinated liquid with a specialized high-resolution and high-readout-speed complementary metal-oxide-semiconductor (CMOS) pixel array, specifically the Topmetal II$^-$ chip, to fabricate a direct conversion X-ray detector. The fluorinated liquid FC40 (molecular formula: $C_{21}F_{48}N_2$) is an electronic medium that is minimally affected by temperature and displays no issues with uniform conductivity. It exhibits a low dark current and minimal radiation damage and enables customizable thickness in X-ray absorption. This addresses the limitations inherent in conventional semiconductor-based detectors. In this study, simple X-ray detector imaging tests were conducted, demonstrating the excellent coupling capability between FC40 electronic fluorinated liquid and CMOS chips by the X-ray detector. A spatial resolution of 4.0 lp/mm was measured using a striped line par card, and a relatively clear image of a cockroach was displayed in the digital radiography imaging results. Preliminary test results indicated the feasibility of fabricating an X-ray detector by combining FC40 electronic fluorinated liquid and CMOS chips. Owing to the absence of issues related to chip-material coupling, a high spatial resolution could be achieved by reducing the chip pixel size. This method presents a new avenue for studies on novel liquid-based direct conversion X-ray detectors.

Keywords FC40 electronic fluorinated liquid · CMOS pixel chip · X-ray detector · Spatial resolution

1 Introduction

X-rays are electromagnetic radiation characterized by high energy and penetration. When X-rays penetrate an object, different materials absorb them to varying degrees. Materials with high density (such as bones) exhibit stronger X-ray absorption than those with low density (such as soft tissue) [1]. X-ray detectors receive the X-rays that penetrate an object and convert them into electrical signals. These collected electrical signals are processed and reconstructed to generate visual X-ray images. The two main types of X-ray detectors are indirect and direct conversion detectors. The former typically uses scintillator materials to convert X-ray signals into photon signals [2, 3]. These photons are then converted into charge signals by a photodetector (such as a photomultiplier tube or photodiode). The latter may experience photon diffusion during the transmission process,

This work was supported by the National Natural Science Foundation of China (No. 12235006) and the National Key Research and Development Program of China (No. 2020YFE0202002.

✉ Xiang-Ming Sun
xmsun@mail.ccnu.edu.cn

✉ Yong-Shuai Ge
ys.ge@siat.ac.cn

1 Key Laboratory of Quark & Lepton Physics (MOE), Central China Normal University, Wuhan 430079, China

2 Guizhou Education University, Guiyang 550018, China

3 Research Center for Medical Artificial Intelligence, Chinese Academy of Sciences, Shenzhen Institutes of Advanced Technology, Shenzhen 518055, China

resulting in a relatively low spatial resolution and potential challenges in capturing fine structures and details [4]. Direct conversion detectors typically use materials with high atomic numbers, such as silicon or selenium. When X-rays penetrate such a detector, their energy is absorbed, creating electron–hole pairs, which are collected by an electric field and converted into charge signals. Direct conversion detectors offer a higher spatial resolution than indirect conversion detectors [5].

To achieve high detection efficiency and spatial resolution, many semiconductor materials, such as amorphous silicon/selenium, cadmium zinc telluride, and perovskites, have been used in direct conversion X-ray detectors. In 1993, the first amorphous silicon flat-panel detector with a PIN structure was proposed [6]. Subsequently, amorphous selenium X-ray detectors using inorganic materials have demonstrated high X-ray sensitivity and spatial resolution, leading to widespread commercial applications [7–9]. However, amorphous selenium detectors are sensitive to temperature changes, and rapid fluctuations ($\geq 5\ °C\ h^{-1}$) can result in crystallization, leading to degraded detector performance or even detachment of the selenium layer or film from the detector surface. Furthermore, a high electric field bias can cause irreparable damage to the detectors [10, 11]. Cadmium telluride zinc (CZT) crystals, which have a large atomic number, high resistivity, and a wide bandgap, are among the most promising room-temperature semiconductor detector materials. Compared with traditional material detectors, they offer advantages such as high-energy resolution, small size, and portability. However, CZT X-ray detectors face challenges in crystal growth and the fabrication of large-area detectors. Furthermore, nonuniform crystal growth results in a nonuniform detector response, directly affecting imaging quality [12]. In recent years, perovskite materials have gained interest as a promising choice for the next generation of direct conversion semiconductor materials in X-ray detectors owing to their high X-ray attenuation coefficient [13–16], long carrier diffusion distance, and radiation stability. However, issues such as dark current and noise caused by ion migration in perovskite materials severely limit the detection limits and operational stability of the devices [17, 18]. Moreover, perovskite materials are susceptible to high-dose radiation damage, leading to decreased sensitivity and performance of the detectors [19, 20]. The fabrication process for perovskite detectors is still under development, and the achievement of large-area high-resolution applications is challenging. In addition, the relatively high cost of perovskite materials may limit their widespread use in certain fields. The complex preparation process of perovskite materials can result in significant performance variations between different detectors, posing challenges for calibration and interchangeability among multiple devices. Regardless of the semiconductor material used in X-ray detectors, none of them are perfect. However, as long as the corresponding application scenarios are identified, further research is worthwhile.

In this study, FC40 electronic fluorinated liquid was employed as a new alternative to address the limitations of traditional semiconductor materials in direct conversion X-ray detectors. These limitations include susceptibility to temperature effects, delamination, nonuniform lattice growth, and vulnerability to radiation damage. FC40 electronic fluorinated liquid is a colorless and transparent perfluorinated chemical with excellent chemical inertness, electrical insulation properties, thermal conductivity, and an extremely low dark current. It is commonly used as a thermal conductive medium in semiconductor manufacturing facilities. Owing to its liquid form, the use of the FC40 fluorinated liquid in the fabrication of X-ray detectors addresses issues such as delamination and radiation damage. Furthermore, the X-ray absorption thickness can be customized to suit specific requirements [21–23]. This novel approach provides possibilities for improving the performance and reliability of direct conversion X-ray detectors by addressing the limitations of traditional semiconductor materials.

2 Materials and methods

2.1 Design of the detector

Figure 1a shows the prototype of a direct conversion X-ray detector using FC40 electronic fluorinated liquid, comprising the detector and readout system. Figure 1b shows the schematic of the direct conversion X-ray detector using FC40 electronic fluorinated liquid, primarily comprising the Topmetal II^{-} chip [24, 25], an FC40 electronic fluorinated liquid device, and a beryllium layer. The top layer of the Topmetal II^{-} chip consists of exposed electrodes, directly in contact with the FC40 electronic fluorinated liquid. The FC40 electronic fluorinated liquid device is fixed to the top metal layer of Topmetal II^{-} using an epoxy resin, creating a cavity of 2 mm (the height can be customized). The top of the cavity is sealed with a 200-μm-thick beryllium layer using epoxy resin, enabling a convenient bias connection. The chip bonding board supplies power, drives the chip, and provides interfaces for connection with the readout board. When X-rays penetrate an object and reach the FC40 electronic fluorinated liquid through the beryllium layer, a reaction occurs. Under the influence of a negative bias voltage, an electric field is generated, causing negative ions to be collected by the Topmetal II pixel array within the electric field. The collected charges are then output through the readout circuit through a polling process.

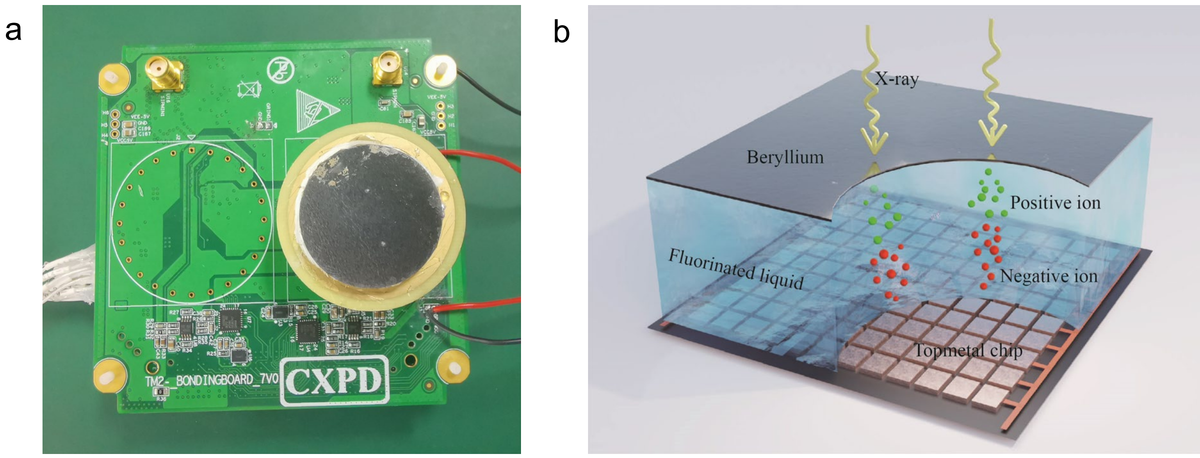

Fig. 1 (Color online) **a** prototype of a detector, with the chip mounted on the driver board that provides power to the chip and interfaces with the readout board. **b** Schematic structure of a direct conversion X-ray detector using FC40 electronic fluoride liquid, consisting of the Topmetal II$^-$ chip, FC40 electronic fluoride liquid device, and beryllium layer

2.1.1 Topmetal chip

The Topmetal II$^-$ chip is a pixel array chip, which collects spatial charges directly using its top metal layer. Each pixel has an exposed metal electrode at the top, enabling the collection of spatial charges generated by the ionization of charged particles. Under the influence of an electric field, these charges drift to the surface of the chip and are collected by the metal electrodes on each pixel, forming a two-dimensional distribution of spatial charges. As shown in Fig. 2, the Topmetal II$^-$ chip consists of a 72×72 pixel array, with a total area of 8 mm $\times$ 9 mm. The area of the charge-sensitive region is 6 mm $\times$ 6 mm. Each pixel has dimensions of 83 μm $\times$ 83 μm, and the size of the top metal electrode exposed to air owing to the opening is 25 μm $\times$ 25 μm. The design noise target for the Topmetal II$^-$ chip is 30 e$^-$. Figure 3a shows the overall structure of a single pixel; the Topmetal II$^-$ chip offers two signal readout modes: analog and digital readout modes. Because these readout modes are independent, the chip can operate in either an analog or a digital readout mode or have all pixel analog readouts connected to a single analog output buffer. In an analog readout mode, scanning the entire pixel array enables the voltage signals from the charge-sensitive amplifiers of each pixel to be read out by the analog output buffer. Alternatively, the signal from any single pixel can be selectively output. The principle of chip simulation readout is shown in Fig. 3b. The digital readout is stored at the bottom of each column and then output through column polling.

ScanModule controls the selection of rows and columns and outputs only the signal from one pixel to the output buffer during a specific time. Each pixel has M_{s1}, M_{s2}, and row select switches (ROW). Each column shares a column select switch (COL). The entire pixel array shares one output

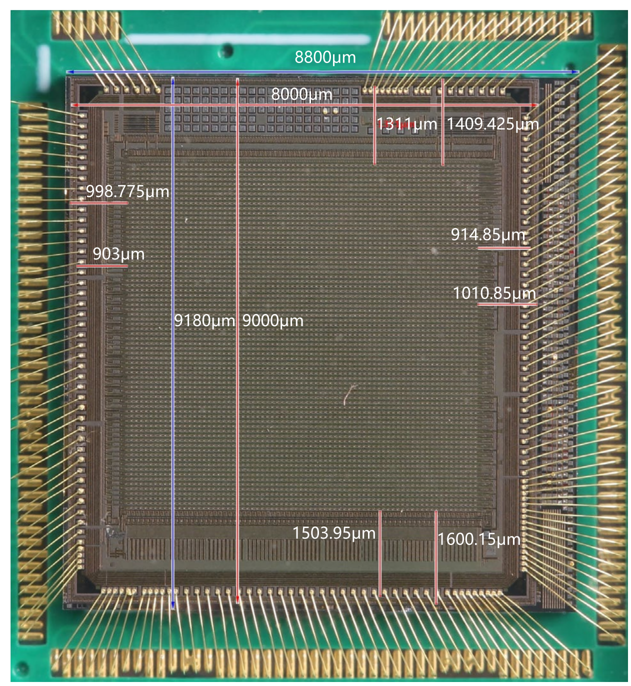

Fig. 2 (Color online) schematic of the wire bonding of the Topmetal II$^-$ chip, where the chip pins are connected to the pads on the bonding board using wire bonds

buffer, M_{r1}, and M_{r2}. The current of the first stage of the source follower, M_{s1} and M_{s2}, is provided to all pixels. However, the second stage of the source follower is used for pixel selection in scanning mode. Because of the limited driving force of charge-sensitive amplifiers within pixels, they can be easily influenced by the row and column switches. The first-stage source follower is necessary to isolate the

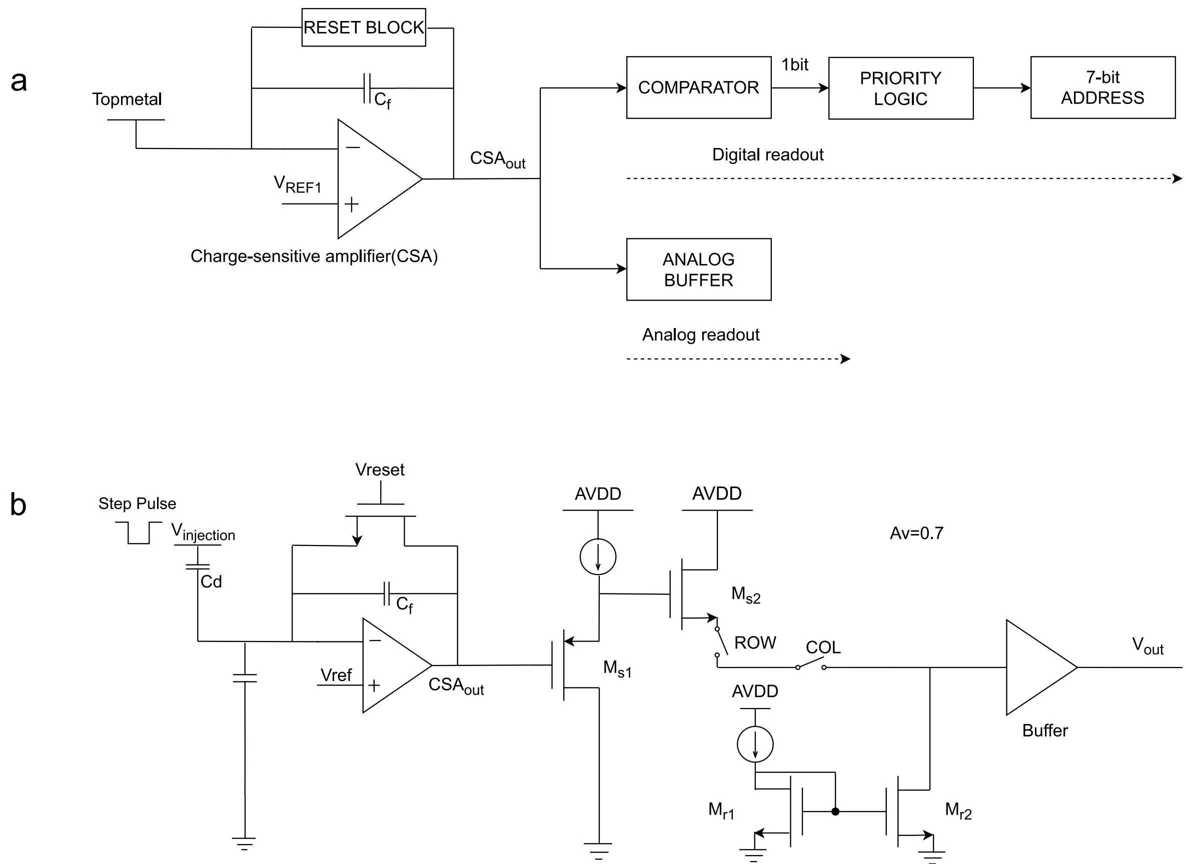

Fig. 3 (Color online) **a** overall structure of a single pixel in the Topmetal II⁻ chip. **b** Principle of the analog readout section of the Topmetal II⁻ chip

row/column selection switches from the charge-sensitive amplifiers [26].

2.1.2 FC40 electronic fluoride liquid

In this study, we attempted to explore the use of electronic fluorinated liquid FC40 as an alternative material for direct conversion X-ray detectors to address the limitations of traditional semiconductor materials. FC40 electronic fluorinated liquid is a colorless and transparent perfluorinated chemical with several advantageous properties including excellent chemical inertness, electrical insulation performance, thermal conductivity, and extremely low dark current. It is commonly used as a thermal conductive medium in semiconductor manufacturing facilities. The temperature range of this liquid extends from −57 to 155 °C, and it has wide applications in etching equipment, ion implantation devices, testing equipment, and other devices. The electrical resistivity of FC40 electronic fluorinated liquid has been determined [27], revealing the IV curve characteristics of the material. A polyethylene container with inner dimensions of 1 cm × 1 cm × 1 cm was used. Copper plates were placed at both ends of the container to serve as electrodes. The container, along with the electronically fluorinated liquid FC40, was placed inside a lead box and exposed to X-ray radiation. The X-ray focus was positioned at a distance of 42.0 mm from the container with X-ray tube settings of 50 kV_p voltage and 100 μA tube current. The objective was to measure the resistivity of FC40 electronic fluorinated liquid under X-ray irradiation.

2.2 Readout system of detector

The back-end signal readout circuit comprises a complementary metal-oxide-semiconductor (CMOS) chip bonding board, mixed-signal conversion board, and control board using a field-programmable gate array (FPGA) [28]. The bonding board houses the bare die of the CMOS chip. Filter capacitors are placed on the bonding board to suppress noise. The bonding board is connected to a mixed-signal conversion board using pin headers. The single-ended analog signals output from the CMOS chip are input to the mixed-signal conversion board and then converted into differential signals to match the input of the analog-to-digital converter (ADS5282, TI, USA). ADS5282 features a 12-bit digital resolution, sampling rate of 65 Msps, and serialized low-voltage differential signaling output interface. A 16-bit digital-to-analog converter (DAC8568, TI, USA) on a mixed-signal conversion board is used to configure the bias voltage of the CMOS chip. The mixed-signal conversion board is connected to the FPGA-based control board using an FPGA mezzanine card connector. The control board, which uses a Xilinx Kintex-7 FPGA, serves as a scalable and minimal hardware core logic controller, including Ethernet transceiver modules, two double-data rates, three synchronous dynamic random-access memory modules (DDR3 SDRAM), and flash configuration modules. The FPGA-based control board receives serialized data output from the ADS5282 and transmits the data to a computer via Ethernet [29–31].

2.3 Digital radiography (DR) imaging platform

The self-developed X-ray DR imaging platform is shown in Fig. 4. It incorporates two types of X-ray sources: a medical-grade X-ray source (Varex G-242, Varex Imaging Corporation, UT, USA) and a micro-focus X-ray source (L9181-02, HAMAMATSU, Japan). Moreover, it includes a horizontal linear stage (model: LS12-X200, Hanjiang, China) with a travel of 200.0 mm and a vertical linear stage (model: STS06-X20, Hanjiang, China) with a travel of 40.0 mm. The medical-grade X-ray tube G-242 has a maximum tube voltage of 125 kV_p and is equipped with a beam collimator to modulate the beam shape using a fixed-beam filter of 1.5 mm aluminum [32]. Spatial resolution testing, modulation transfer function (MTF) evaluations, and PCB DR images were obtained using the medical-grade G-242 X-ray source, and

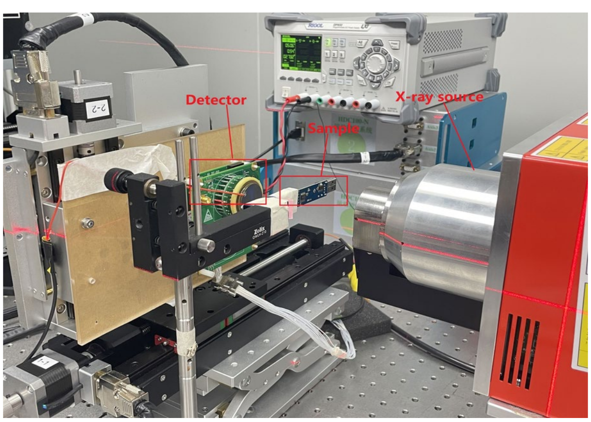

Fig. 4 (Color online) custom-built large light source X-ray (or micro-focus X-ray) digital radiography (DR) imaging platform, where the test object and detector are placed on a motion platform for vertical and horizontal movements. Spatial resolution, modulation transfer function (MTF), noise power spectrum (NPS), and DR imaging are performed on this platform

noise power spectrum (NPS) and cockroach DR images were obtained using the micro-focus X-ray source. The detector enabled continuous scanning along the vertical and horizontal directions on the linear stages, enabling rapid imaging of samples larger than 5 cm × 10 cm. Specific experimental parameter settings for each test group are presented in the Results section. Multiple X-ray projection images obtained from the CMOS were post-processed and stitched together to form complete DR projections of objects. In particular, signals corresponding to the same spatial positions were combined, whereas those corresponding to different spatial positions were systematically rearranged [33, 34]. For comparison, MTF and NPS measurements were conducted using a commercial scintillator (CsI:TI)-based indirect conversion CMOS flat-panel detector (model: Dexela 2329 NDT, PerkinElmer, USA). Notably, the experiment did not adhere to IEC standards because of the prototype nature of the CMOS direct conversion X-ray detector coupled with a fluorinated liquid, which had a small size (72 × 72 pixels), preventing compliance with IEC measurement protocols and imposing restrictions on distance measurements. The experiments were conducted under identical conditions to ensure comparable results.

3 Experimental results

3.1 Electronic properties of FC40 electronic fluorinated liquid

To understand the electronic characteristics of FC40 electronic fluorinated liquid, the IV (current–voltage) curve was measured using the test setup shown in Fig. 5a. The FC40 electronic fluorinated liquid exhibited an ideal linear current response under X-ray radiation. With the X-ray tube current maintained at 100 μA, the tube voltage was scanned at bias voltages of 100, 150, and 200 V. As shown in Fig. 5b, the current response of the FC40 electronic fluorinated liquid was susceptible to high tube voltages.

3.2 Spatial resolution

The spatial resolution was obtained by acquiring standard striped pattern DR images of the line-pair card (model: Type 18-d, QUART GmbH, Germany) through continuous exposure to a medical-grade X-ray tube (G-242, Varex Imaging Corporation, USA). The X-ray tube was operated at 50 kV_p with a tube current of 12.5 mA. The distance from the X-ray focal spot to the center of the line-pair card was 474.0 mm and that from the X-ray focal spot to the photosensitive layer of the CMOS detector was 476.0 mm. While keeping the line-pair card stationary, the detector moved at a speed of 3.0 mm/s in the vertical direction. The image of the line-pair

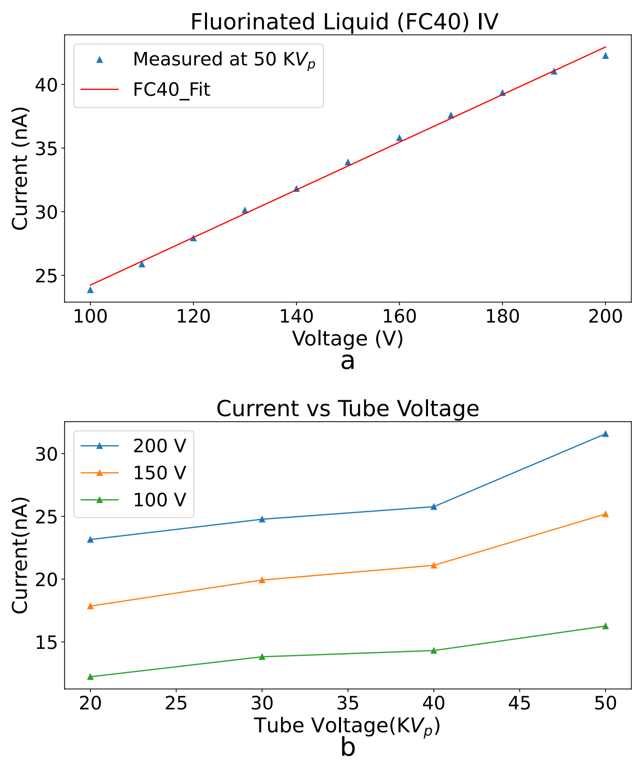

Fig. 5 (Color online) **a** IV curve of FC40 electron fluorination liquid under X-ray irradiation at 50 kV$_p$, with a bias voltage range of 100 to 200 V, corresponding to an electric field increasing from 100 to 200 V/cm. **b** X-ray tube voltage scanning at bias voltages of 100, 150, and 200 V

card obtained by stitching is shown in Fig. 6a, demonstrating the capability of the fluorinated liquid detector to resolve structures with spatial frequencies greater than 4.0 lp/mm.

3.3 MTF

The MTF measurement was performed using a medical-grade G-242 X-ray source operating at a tube voltage of 50 kV$_p$ and tube current of 12.5 mA. A 1.0 mm tungsten plate was tilted at 3° and secured onto a linear horizontal stage. The distance from the X-ray focal point to the tungsten plate was 638 mm and that from the tungsten plate to the surface of the CMOS detector was 2.0 mm. The tungsten plate remained stationary while the detector moved horizontally and vertically at a speed of 1.0 mm/s, capturing 5000 frames per scan and conducting a total of 10 scans. The experiment employed the tilted edge method to measure the edge spread function (ESF) for fine sampling. Subsequently, the ESF was differentiated to obtain the line spread function (LSF). The obtained LSF underwent a fast Fourier transform, and its value at zero spatial frequency was normalized to compute the MTF [35, 36]. Under the same experimental conditions, compared with the commercial indirect conversion Dexela

Table 1 Detector characteristics

Design feature	FC40 detector	Dexela 2923N detector
Pixel size (μm)	83	74.8
Array size	72 × 72	3888 × 3072
Sensitive area (mm^2)	6 × 6	290.8 × 229.8
Material thickness (μm)	2000	500
Detector type	Direct conversion	Indirect conversion
Material	FC40	CsI

2329 NDT detector, the FC40 electronic fluorinated liquid detector exhibited superior MTF at low frequencies, as shown in Fig. 6b. This demonstrates an advantage of the FC40 electronic fluorinated liquid material in direct conversion applications. The parameters of the FC40 electronic fluorinated liquid detector and the Dexela 2329 detector are presented in Table 1.

3.4 NPS

NPS measurements were conducted using a micro-focus X-ray source (L9181-02, HANAMATSU, Japan) with a tube voltage of 50 kV$_p$ and tube current of 0.1 mA. A PCB was fixed on a horizontal linear stage, with the distance from the X-ray focal point to the surface of the CMOS detector at 159 mm and that from the PCB to the CMOS detector at 82 mm. While maintaining the PCB stationary, the detector moved at a speed of 2.0 mm/s in both the vertical and horizontal directions, collecting 8000 frames per scan. The resulting NPS curve was not ideal, as shown in Fig. 6c, indicating a certain level of correlation within the CMOS detector. Under identical experimental conditions, it might exhibit slightly weaker characteristics than the current Dexela commercial detector, particularly displaying a reduced correlation at high frequencies. This could potentially be attributed to the direct conversion process, where, because of the thickness of the material, ion drifting might cause some cross talk among ions arriving at different pixels on the detection surface [37, 38].

3.5 Signal to noise ratio (SNR)

To measure the SNR, a 2.0-mm aluminum plate and 4.5-mm PMMA plate were stacked non-overlapped and fixed on a horizontal platform. The distance from the X-ray focal point to the surface of the CMOS detector was 476.0 mm and that from the PMMA plate to the CMOS detector was 76 mm. The PMMA plate remained stationary while the detector moved at a speed of 3.0 mm/s in both the vertical and horizontal directions, acquiring 5000 frames per movement. The CMOS detector was biased at −3 kV, and the chip Vrest was set at 700 mV. Six tube currents and their

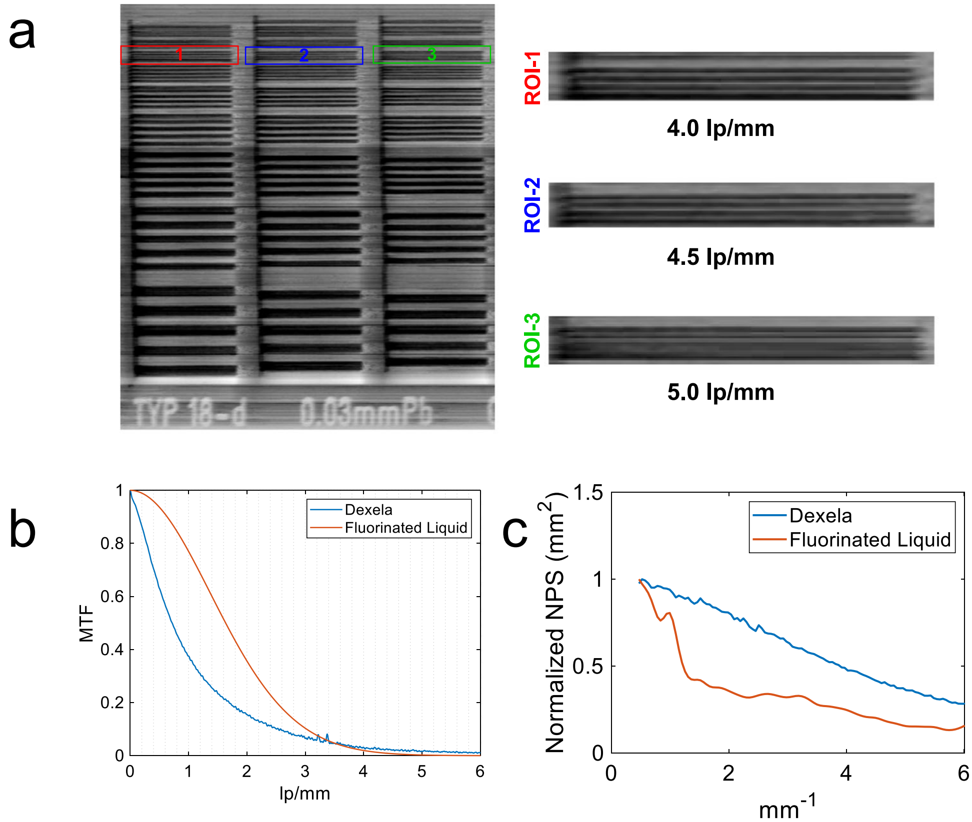

Fig. 6 (Color online) **a** spatial resolution of the FC40 electronic fluorinated liquid detector was tested using QUART GmbH line-pair patterns. The spatial resolution stripes of ROI-1 (4.0 lp/mm) can be distinguished. However, the regions of ROI-2 (4.5 lp/mm) and ROI-3 (5.0 lp/mm) appear more blurred. **b** MTF was measured using X-rays at a tube voltage of 50 kV_p and 12.5 mA and compared with the MTF response curve of the commercial Dexela detector. **c** NPS was obtained by imaging a PCB using a micro-focus X-ray source at 50 kV_p and 0.1 mA and subsequently compared with the NPS response curve of the commercial Dexela detector

corresponding dose rates were scanned six times using a medical-grade G-242 X-ray source with a tube voltage of 50 kV. The detector moved at a speed of 3 mm/s on a vertical linear stage for each scan, collecting 5000 frames per scan. Because of excessive experimental interference, the obtained experimental results were unsatisfactory, and the SNR results were not computed [39].

3.6 DR imaging results

The tube voltage of the micro-focus X-ray source was set to 20 kV_p, with a tube current of 200 μA. The cockroach was placed inside a transparent plastic bag and suspended on a platform. The distance from the X-ray focal point to the CMOS detector was 159.0 mm and that from the cockroach to the CMOS detector was 82.0 mm. Keeping the cockroach stationary, the detector moved at a speed of 3.0 mm/s in both the vertical and horizontal directions, collecting 10,000 frames per movement. The stitched DR image of the cockroach obtained through this process is shown in Fig. 7a, displaying a clear resolution of the spines on the legs of the cockroach.

The tube voltage for the medical-grade G-242 X-ray source was set to 50 kV_p, with a tube current of 12.5 mA. A PCB was fixed onto a horizontal linear stage, with the distance from the X-ray focal point to the CMOS detector set to 204.0 mm and that from the PCB to the CMOS detector set to 43.0 mm. While maintaining the PCB stationary, the detector moved at a speed of 3.0 mm/s in both the vertical and horizontal directions, collecting 6000 frames per movement. The stitched DR image of the PCB obtained after this process is shown in Fig. 7b, displaying a clear resolution of the pin information of the chip on the PCB.

4 Conclusion

In this study, a CMOS direct conversion X-ray detector coupled with FC40 electronic fluorinated liquid was developed. The setup employed a specialized high-resolution and high-readout speed CMOS pixel array, the Topmetal II^- chip, coupled with FC40 fluorinated liquid. FC40, an electronic fluorinated liquid, circumvents performance issues, such as delamination and uneven crystal growth, observed in traditional semiconductor materials, offering the advantage of customizable X-ray absorption thickness. To validate the feasibility of coupling CMOS chips with this liquid arrangement and offer a new direction for researching novel liquid direct conversion X-ray detectors, preliminary experiments demonstrated imaging performances consistent with expectations. The spatial resolution reached 4.0 lp/mm, showing an advantage in the low-frequency domain

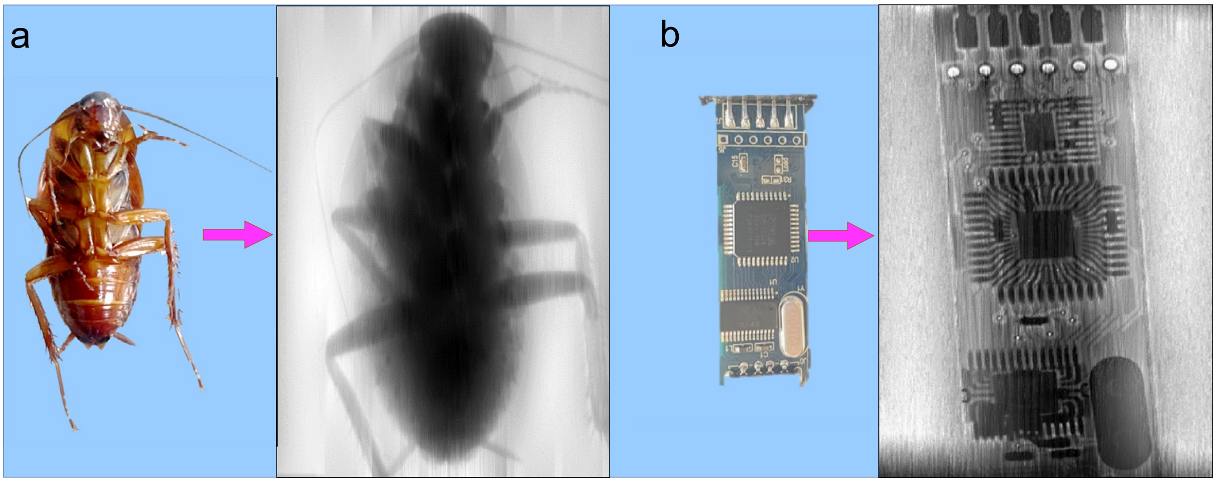

Fig. 7 (Color online) **a** detector displaying the image of a cockroach using a micro-focus X-ray source (HAMAMATSU) operating at a tube voltage of 20 kV_p and tube current of 200 μA, revealing the spines on the cockroach's legs. **b** Detector displaying the image of a PCB using a medical-grade G-242X X-ray source (Varex) with settings of 50 kV_p and 12.5 mA, resulting in a stitched PCB DR image that distinctly delineates the chip pins on the PCB

for MTF compared with commercial Dexela scintillator indirect detectors under the same experimental conditions. However, because of the design-related thickness of the fluorinated liquid layer, the NPS did not meet expectations. The experiments also produced relatively visible DR images of the cockroach and PCB. These preliminary findings demonstrate the viability of using FC40 electronic fluorinated liquid coupled with CMOS chips to fabricate X-ray detectors. This alternative approach to traditional semiconductor materials has distinct advantages when coupled with CMOS chips, presenting an extremely low dark current and negligible radiation damage. These characteristics suggest promising potential applications in low-energy and high-radiation environments.

However, some limitations are also associated with CMOS fluorinated liquid X-ray detectors. The slow charge migration resulting from the use of FC40 electronic fluorinated liquid, which is inert, may limit the response speed and sensitivity of the detector. Additionally, because of the relatively low atomic number of FC40 electronic fluorinated liquid, its ability to block X-rays is comparatively weak. Consequently, the performance of CMOS fluorinated liquid detectors may be constrained in high-energy X-ray detection.

Future studies will investigate the electrical characteristics of the FC40 fluorinated liquid and explore methods to test the charge-transfer efficiency. Moreover, to leverage its advantages when coupled with CMOS chips, further research can focus on combining FC40 with smaller pixel Topmetal chips to create high-precision X-ray detectors that are suitable for low-energy applications. This will assist in expanding the application prospects of CMOS fluorinated liquid detectors in areas such as medical imaging, materials analysis, and other low-energy and high-radiation detection fields. The investigation of the electrical properties of FC40 and the development of improved detector designs will contribute to enhancing the performance and capabilities of CMOS fluorinated liquid detectors. Further studies and development will enable the exploration of new applications and advancements in the field of X-ray detection.

Author Contributions All authors contributed to the study conception and design. Material preparation, data collection, and analysis were performed by Shi-Hua Liu, Xin Zhang, Meng Wu, Zhi-Hui Han, and Tong Wan. The first draft of the manuscript was written by Shi-Hua Liu, and all authors commented on previous versions of the manuscript. All authors read and approved the final manuscript.

Data availability The data that support the findings of this study are openly available in Science Data Bank at https://cstr.cn/31253.11.sciencedb.j00186.00129 and https://doi.org/10.57760/sciencedb.j00186.00129.

Declarations

Conflict of interest The authors declare that they have no conflict of interest.

References

1. Z. Li, F. Zhou, H. Yao et al., Halide perovskites for high-performance X-ray detector. Mater. Today **48**, 155–175 (2021). https://doi.org/10.1016/j.mattod.2021.01.028
2. C. Zhang, W. Dou, X. Yang et al., X-ray detectors based on Ga_2O_3 microwires. Materials **16**, 4742 (2023). https://doi.org/10.3390/ma16134742

3. M. Chen, Z. Zhang, R. Zhan et al., Fast-response X-ray detector based on nanocrystalline Ga_2O_3 thin film prepared at room temperature. Appl. Surf. Sci. **554**, 149619 (2021). https://doi.org/10.1016/j.apsusc.2021.149619
4. F. Zhou, Z. Li, W. Lan et al., Halide perovskite, a potential scintillator for X-ray detection. Small Methods **4**, 2000506 (2020). https://doi.org/10.1002/smtd.202000506
5. M. Spahn, X-ray detectors in medical imaging. Nucl. Instrum. Methods A **731**, 57–63 (2013). https://doi.org/10.1016/j.nima.2013.05.174
6. R. Street, Semiconductor of distinction. Phys. World **6**, 54 (1993). https://doi.org/10.1088/2058-7058/6/4/27/meta
7. S. Yuan, L. Wang, F. Liu et al., Early crystallization of amorphous selenium under high pressure studied by synchrotron XRD method. J. Phys. Condens. Matter. **35**, 264003 (2023). https://doi.org/10.1088/1361-648X/acc8b0
8. X. Ou, X. Chen, X. Xu et al., Recent development in X-ray imaging technology: future and challenges. Research **2021**, 9892152 (2021). https://doi.org/10.34133/2021/9892152
9. Y. He, I. Hadar, M.G. Kanatzidis, Detecting ionizing radiation using halide perovskite semiconductors processed through solution and alternative methods. Nat. Photon. **16**, 14–26 (2022). https://doi.org/10.1038/s41566-021-00909-5
10. Y. Wang, H. Lou, C.Y. Yue et al., Applications of halide perovskites in X-ray detection and imaging. CrystEngComm **24**, 2201–2212 (2022). https://doi.org/10.1039/D1CE01575C
11. Z.H. Warsi, Design, Fabrication and characterization of a unipolar charge sensing amorphous selenium X-ray detector. Dissertation, University of Waterloo, 2023. http://hdl.handle.net/10012/19561
12. Y. Yuan, S. Xie, C. Ding et al., Fabricating flexible wafer-size inorganic semiconductor devices. J. Mater. Chem. C **8**, 1915–1922 (2020). https://doi.org/10.1039/C9TC05781A
13. D.L. Wang, H.J. Cui, G.J. Hou et al., Highly efficient light management for perovskite solar cells. Sci. Rep. **6**, 18922 (2016). https://doi.org/10.1038/srep18922
14. Z. Wang, S. Tie, H. Zhang et al., Supple formamidinium-based low-dimension perovskite derivative for sensitive and ultrastable X-ray detection. ACS Nano. **17**, 13638–13647 (2023). https://doi.org/10.1021/acsnano.3c02476
15. Y. Tan, G. Mu, M. Chen et al., X-ray detectors based on halide perovskite materials. Coatings **13**, 211 (2023). https://doi.org/10.3390/coatings13010211
16. W. Li, D. Xin, S. Tie et al., Zero-dimensional lead-free $FA_3Bi_2I_9$ single crystals for high-performance X-ray detection. J. Phys. Chem. Lett. **12**, 1778–1785 (2021). https://doi.org/10.1021/acs.jpclett.1c00090
17. S. Zhao, X. Du, J. Pang et al., Dark current modeling of thick perovskite X-ray detectors. Front. Optoelectron. **15**, 43 (2022). https://doi.org/10.1007/s12200-022-00044-1
18. J. Peng, Y. Xu, F. Yao et al., Thick-junction perovskite X-ray detectors: processing and optoelectronic considerations. Nanoscale **14**, 9636–9647 (2022). https://doi.org/10.1039/D2NR01643E
19. Q. He, C. Zhou, L. Xu et al., Highly stable organic antimony halide crystals for X-ray scintillation. ACS. Mater. Lett. **2**, 633–638 (2020). https://doi.org/10.1021/acsmaterialslett.0c00133
20. B. Yang, L. Yin, G. Niu et al., Lead-free halide Rb_2CuBr_3 as sensitive X-ray scintillator. Adv. Mater. **31**, 1904711 (2019). https://doi.org/10.1002/adma.201904711
21. N.S. Bhairamadgi, S.P. Pujari, C.J.M. van Rijn et al., Adhesion and friction properties of fluoropolymer brushes: on the tribological inertness of fluorine. Langmuir **30**, 12532–12540 (2014). https://doi.org/10.1021/la501802b
22. H. Kajikawa, H. Iizumi, T. Kobata, Using volatile liquid FC-40 as pressure transmitting medium for pressure gauge calibrations. J. Phys. Conf. Ser. **1065**, 162009 (2018). https://doi.org/10.1088/1742-6596/1065/16/162009/meta
23. M. Muneeshwaran, Y.C. Lin, C.C. Wang, Performance analysis of single-phase immersion cooling system of data center using FC-40 dielectric fluid. Int. Commun. Heat Mass Transf. **145**, 106843 (2023). https://doi.org/10.1016/j.icheatmasstransfer.2023.106843
24. C. Gao, G. Huang, X. Sun, Topmetal-II-: a direct charge sensor for high energy physics and imaging applications. JINST. **11**, C01053 (2016). https://doi.org/10.1088/1748-0221/11/01/C01053/meta
25. M.M. An, C. Chen, C. Gao et al., A low-noise CMOS pixel direct charge sensor, topmetal II. Nucl. Instrum. Methods Phys. Res. A. **810**, 144–150 (2016). https://doi.org/10.1016/j.nima.2015.11.153
26. W.P. Ren, W. Zhou, B.H. You et al., Topmetal-M: a novel pixel sensor for compact tracking applications. Nucl. Instrum. Meth. A **981**, 164557 (2020). https://doi.org/10.1016/j.nima.2020.164557
27. H. Ahmad, W. Balachandran, N. Manivannan, Measurement of electrical resistivity of hydrofluorocarbons —a review. J. Electrost. **109**, 103546 (2021). https://doi.org/10.1016/j.elstat.2020.103546
28. H. Wang, D. Wang, R. Chen et al., Electronics system for the cosmic X-ray polarization detector. Nucl. Sci. Tech. **34**, 64 (2023). https://doi.org/10.1007/s41365-023-01221-3
29. Z. Li, H. Feng, X. Huang et al., Preliminary test of topmetal-II sensor for X-ray polarization measurements. Nucl. Instrum. Meth. A **1008**, 165430 (2021). https://doi.org/10.1016/j.nima.2021.165430
30. S.G. Zou, Y. Fan, X.M. Sun et al., A highly pixelated CdZnTe detector based on topmetal II-sensor. Chin. Phys. C **41**, 046003 (2017). https://doi.org/10.1088/1674-1137/41/4/046003/meta
31. R. He, X.Y. Niu, Y. Wang et al., Advances in nuclear detection and readout techniques. Nucl. Sci. Tech. **34**, 205 (2023). https://doi.org/10.1007/s41365-023-01359-0
32. Y. Liu, C. Gao, J. Zhu et al., CMOS based high-resolution dynamic X-ray imaging with inorganic perovskite. (2022). https://doi.org/10.48550/arXiv.2210.02073
33. W.J. Sun, S. Chretien, A. Biguri et al., The realisation of fast X-ray computed tomography using a limited number of projection images for dimensional metrology. NDT E Int. **137**, 102852 (2023). https://doi.org/10.1016/j.ndteint.2023.102852
34. Y. Ge, T. Su, J. Zhu et al., ADAPTIVE-NET: deep computed tomography reconstruction network with analytical domain transformation knowledge. Quant. Imaging Med. Surg. **10**, 415–417 (2020). https://doi.org/10.21037/qims.2019.12.12
35. S. Zhang, F. Wang, X. Wu et al., MTF measurement by slanted-edge method based on improved Zernike moments. Sensors **23**, 509 (2023). https://doi.org/10.3390/s23010509
36. T.C. Li, X.P. Tao, H.J. Feng et al., Modulation transfer function calculation and image restoration based on slanted-edge method. Acta. Optica. Sinica. **30**, 2891 (2010). https://doi.org/10.3788/aos20103010.2891
37. T.S. Wang, X. Liu, J.J. Dai et al., An unsupervised dual contrastive learning framework for scatter correction in cone-beam CT image. Comput. Biol. Med. **165**, 102852 (2023). https://doi.org/10.1016/j.compbiomed.2023.107377
38. C. Yang, W.Z. Wang, D.Y. Cui et al., Deep learning image reconstruction algorithms in low-dose radiation abdominal computed tomography: assessment of image quality and lesion diagnostic confidence. Quant. Imaging Med. Surg. **13**, 3161–3173 (2023). https://doi.org/10.21037/qims-22-1227
39. M.J. Firbank, A. Coulthard, R.M. Harrison et al., A comparison of two methods for measuring the signal to noise ratio on MR

images. Phys. Med. Biol. **44**, N261 (1999). https://doi.org/10.1088/0031-9155/44/12/403/meta